Synthesis and Description of Small Gold and Palladium Nanoparticles on CeO₂ Substrate: FT- IR Spectroscopy Data

A. A. Tereshchenko[a], *, V. A. Polyakov[a, b], A. A. Guda[a], **, A. N. Bulgakov[a], A. L. Tarasov[c],
L. M. Kustov[c], V. V. Butova[a, b], A. L. Trigub[d], and A. V. Soldatov[a]

[a] *The Smart Materials Research Institute, Southern Federal University, Rostov-on-Don, 344090 Russia*
[b] *Southern Scientific Center, Russian Academy of Sciences, Rostov-on-Don, 344006 Russia*
[c] *Zelinsky Institute of Organic Chemistry, Russian Academy of Sciences, Moscow, 119991 Russia*
[d] *National Research Center "Kurchatov Institute", Moscow, 123182 Russia*
*e-mail: tereshch1@gmail.com
**e-mail: guda_sasha@mail.ru

Abstract—Palladium (Pd/CeO₂), gold (Au/CeO₂), and bimetallic (PdAu/CeO₂) nanoparticles obtained via impregnation of the surface of cerium dioxide with tetraethylene pentamine and subsequent reduction in a H₂/Ar flow are synthesized and described. The particles possess a high degree of dispersion, but their small size complicates their analysis with conventional methods (transmission electron microscopy and X-ray powder diffraction). Diffuse reflectance infrared Fourier transform spectroscopy (DRIFTS) combined with CO sample molecules is used to study the size and morphology of the nanoparticles and the substrate. The intensity ratios of the bands assigned to bridge and linear carbonyls at palladium centers indicate that there are finely divided nanoparticles in the case of a monometallic sample and larger nanoparticles in the case of a bimetallic one. The resulting materials have high catalytic activity and stability: the complete conversion of CO for Pd/CeO₂ is achieved at about 50°C. We find that the catalytic activity of the samples decreases in the series Pd/CeO₂–Au/CeO₂–PdAu/CeO₂, which indicates that there is no synergistic effect in the case of a bimetallic sample.

Keywords: catalysts, nanoparticles, palladium, gold, cerium dioxide substrate, tetraethylene pentamine, CO oxidation, adsorption, diffuse reflectance Fourier transform infrared spectroscopy (DRIFTS), sample molecules, carbon monoxide

DOI: 10.1134/S1027451020030180

INTRODUCTION

Noble-metal nanoclusters are known as catalysts for various hydrogenation and oxidation reactions, in particular CO oxidation. A catalyst based on palladium and/or gold nanoparticles on various substrates, which is highly active at low temperatures, has been synthesized several times [1–8]. The catalytic activity of nanoparticles depends on their size and shape [9], substrate material [10], functionalization [11], and composition [12]; in addition, the most important factors for the high catalytic activity of nanoparticles are their high dispersion and uniform distribution over the surface of a substrate [13]. One way is to use matrix surfaces as substrates modified, for example, via the deposition of palladium onto a SiO₂ substrate [14]. Silica gel was synthesized in situ with simultaneous surface modification via the introduction of 3-aminopropyltriethoxysilane into the system. The precursor salts were reduced with an aqueous solution of sodium borohydride. When modified silica gel was used, pal-

ladium nanoparticles 1.5–2 nm in size were obtained. The particle size appeared to be much larger (4–5 nm) in the case of an unmodified surface. The authors assumed that this was due to stronger interaction between palladium ions and the surface modified.

FDU−15 mesoporous carbon was used as a matrix, whose surface was modified by two different methods: heating in a flow of gaseous ammonia (ammonolysis) and treatment of the substrate with melamine during heating [15]. The precursor salts were reduced with sodium borohydride. The smallest palladium particles were obtained via ammonolysis, and their size was from 1 to 3 nm. When melamine was used, nanoparticles 3–4 nm in size were formed.

The electrostatic adsorption method was also used to synthesize ultrafine bimetallic nanoparticles of various compositions (Pt−Pd, Pd−Co, Pd−Cu, Cu−Ni, etc.). The charged ions of the metal precursors were effectively adsorbed on oppositely charged surfaces via adjustment of the pH relative to the zero charge point

of the surface [16]. Silica gel was impregnated with ammonia complexes of precursor salts (hexaamine nickel chloride(II), tetraamine copper(II) nitrate, hexaamine cobalt(III) chloride, tetraamine platinum(II) hydroxide, and tetraamine palladium(II) chloride). Then the materials were treated in a hydrogen flow at 400°C, and bimetallic clusters with 1–1.5 nm in size were obtained.

There is a method, which implies that palladium nanoparticles coated with polyvinylpyrrolidone or hydroxypolyamidamine react to form in situ silica gel from triethoxysilane and 1,2-bis(triethoxysilyl)ethane [17]. This approach was used to obtain palladium nanoparticles 1–4 nm in size. There are also several methods for modification of the surface of cerium dioxide, which can be divided into in situ and postsynthetic types. In particular, the first is a technique, where modifier molecules (hexadecyltrimethylammonium bromide, cetylpyridinium bromide etc.) were introduced, when cerium dioxide was formed [18]. In this case, such cationic modifiers were chosen due to the anionic function of the intermediate oxidation product of Ce^{3+} ions—cerium hydroxide. Postsynthetic modifications are described in [19, 20]. Cerium dioxide synthesized preliminarily was treated with a solution of nitric acid [19]. A surface of nanoparticles containing nitro groups was obtained. A method for the ammonolysis of a CeO_2 film at various temperatures is described, after which nitrogen atoms replace the surface oxygen atoms of nanoparticles [20].

Two methods for the synthesis of gold nanoparticles on cerium dioxide were used [21]. The first method is in-situ coprecipitation by mixing aqueous solutions of tetrachloro-tartaric acid and cerium-ammonium nitrate. After this, the pH of the solution was 8, and the resulting precipitate was collected and calcined at 400°C. The second method is impregnation of the final substrate. Gold-containing acid was precipitated on a CeO_2 substrate already prepared and calcined. The sample obtained via coprecipitation contained larger gold nanoparticles, up to ~8 nm. The impregnated material contained gold particles less than 5 nm in size. The authors assume that this effect is due to the calcination process, when small particles sinter into larger agglomerates. The resulting materials were studied as catalysts for the conversion of a CO/H_2O mixture.

Palladium and gold nanoparticles were synthesized on various substrates via impregnation and reduction in polyethylene glycol under microwave radiation [3]. In this case, polyethylene glycol acts as an effective absorber of microwave radiation due to its high dielectric constant. A supersaturated metal solution is formed during rapid and uniform heating. The higher the supersaturation, the higher the nucleation rate and the lower the critical sizes of nuclei needed to overcome the nucleation barrier. In addition, rapid microwave heating provides a uniform temperature and the necessary ion concentration for nucleation and growth.

The Au/CeO_2 catalyst was synthesized via impregnation of the final substrate under supercritical conditions [1]. As a result, gold clusters 1–10 nm in size were formed. There is also another method to obtain such materials. Palladium and gold nanoparticles and their bimetallic clusters were synthesized on a cerium-dioxide substrate via laser evaporation and controllable condensation [2]. This method does not imply the chemical transformations of materials, but is based on the evaporation/condensation of final metal powders and their oxides. Palladium and gold nanoparticles with a size of 5–10 nm were obtained. The materials exhibited high catalytic activity in the oxidation of CO.

Palladium and gold nanoparticles and their bimetallic compounds are synthesized on a modified surface of cerium dioxide in this work. This material is an active substrate capable of supplying oxygen from the crystal lattice to provide oxidation reactions [22]. Cerium-dioxide nanoparticles are treated with an aqueous solution of tetraethylene pentamine (TEPA) containing primary and secondary amino groups. The resulting surface possesses electron-donor properties and better sorb the positively charged noble-metal ions.

Tetraammine palladium(II) chloride was chosen as a palladium precursor. This was due to two reasons: firstly, ammonium complex salts of noble metals are highly soluble in water and do not undergo hydrolysis in comparison with non-complex chlorides; secondly, ammonia complexes have a higher affinity for amino groups. These factors contribute to the efficient adsorption of noble-metal ions on the surface, whereas a large number of nucleation centers leads to a decrease in size of the resulting nanoparticles. A complex anionic chloride, sodium tetrachloroaurate(III), is chosen as a gold precursor in contrast to a palladium one. This is due to the instability of gold(III) cationic ammonia complexes in an aqueous medium, and the tetrachloroaurate ion is very stable and is not hydrolyzed even at higher temperatures. The main methods conventionally used to describe noble metals (X-ray powder diffraction and transmission electron microscopy) have some limitations in the study of nanoparticles on substrates with a high charge number, which is typical for cerium dioxide (low Z-contrast). We show that Fourier-transform infrared (IR) spectroscopy together with CO as sample molecules is an effective technique to describe such samples [23–25].

EXPERIMENTAL

Materials

99.5% cerium(III) nitrate hexahydrate (Alfa Aesar), 99.999% palladium(II) chloride (Alfa Aesar), 99.99% sodium tetrachloroaurate(III) dihydrate (Alfa Aesar), 28–30% ammonium hydroxide (Alfa Aesar),

Table 1. Amount of reagents used in synthesis

| Sample	Precursor salt	Amount of precursor, mmol	Weight of CeO_2/TEPA, mg
Pd/CeO_2	$[Pd(NH_3)_4]Cl_2$	0.0505	129
Au/CeO_2	$Na[AuCl_4] \cdot 2H_2O$	0.0317	150
PdAu/CeO_2	$[Pd(NH_3)_4]Cl_2$	0.0177	129
	$Na[AuCl_4] \cdot 2H_2O$	0.0177	

98% tetraethylene pentamine pentahydrochloride (TEPAPHC) (Alfa Aesar), 99% sodium chloride (Alfa Aesar), 99.5% sodium carbonate anhydrous (Alfa Aesar), and 99.9995% silver nitrate (Alfa Aesar) were used to prepare the substrates and catalysts. Methanol (J.T. Baker Ultra Pure) was used without further purification.

### Synthesis of a Modified Substrate

Cerium-dioxide nanoparticles were synthesized as described in [26]. 10% solution of TEPAPHC was prepared via its 1.11 g dissolution in 10 ml of distilled water to modify the surface of cerium-dioxide nanoparticles. A concentrated ammonia solution was added dropwise to the resulting solution to reach a pH of 7—8. Then 1 g of cerium dioxide synthesized was suspended in TEPA solution. The suspension was thoroughly mixed for 2 h and then washed four times with distilled water via centrifugation (15000 rpm). The resulting material was dried in air at room temperature. The modified cerium-dioxide substrate is then designated as CeO_2/TEPA.

Synthesis of Noble-Metal Nanoparticles

Tetraamine palladium (II) chloride was synthesized from $PdCl_2$. Palladium(II) chloride was dissolved in a saturated aqueos solution of sodium chloride; 5% ammonia was added to the resulting red-brown solution to reach a pH of 10—11. Yellow palladium(II) diamine chloride crystals formed:

$$Na_2[PdCl_4] + 2NH_3 \cdot H_2O_{dil} = [Pd(NH_3)_2Cl_2] \downarrow + 2H_2O + 2NaCl. \quad (1)$$
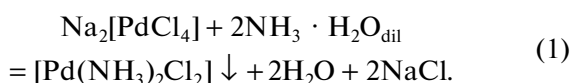
The precipitate was washed with distilled water until the chloride ions were completely removed (test with $AgNO_3$) and dried at 60°C. The resulting compound was dissolved in a minimum volume of concentrated ammonia solution to form a colorless solution:

$$[Pd(NH_3)_2Cl_2] + 2NH_3 \cdot H_2O_{conc} = [Pd(NH_3)_4]Cl_2 + 2H_2O. \quad (2)$$
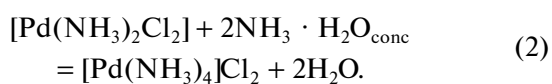
The solution was evaporated at room temperature. Colorless tetraammine palladium(II) chloride crystals formed.

A metal precursor sample was dissolved in 12.5 mL of distilled water. The solution was heated to 60°C during stirring, and then CeO_2/TEPA was added. The resulting suspension was stirred for 30 minutes, and then 0.2-M sodium carbonate solution was added to pH 8. The mixture was stirred for 1 h, centrifuged, and washed three times with distilled water until a negative reaction occurred for chloride ions in wash waters ($AgNO_3$ test). The material washed was dried for a night at 60°C. Then the material was placed into a tubular furnace in porcelain boats and heated to 350°C in a flow of pure argon (50 mL/min). The argon flow was replaced with a mixture of 5% H_2 and 95% Ar for a constant total flow. The material was kept for 1 h under such conditions, and then the system was cooled to room temperature in a flow of pure argon (50 mL/min). The theoretical amount of metal was 4 wt %.

The gold-containing sample was synthesized in a similar way with sodium tetrachloroaurate(III) dihydrate as a precursor and 4 wt % of gold. The bimetallic (PdAu) sample, in which tetraamine palladium(II) chloride and sodium tetrachloroaurate(III) dihydrate were used as precursors (amount of gold and palladium metals was 2 wt %) was also obtained. These materials are designated as Pd/CeO_2, Au/CeO_2, and PdAu/CeO_2. Table 1 shows the amounts of the reagents used.

Methods

X-ray fluorescence spectra were acquired on a Bruker M4 Tornado spectrometer (United States) equipped with an XFlash 430 detector in the energy range from 0 to 24 keV. X-ray powder diffraction patterns were obtained on a Bruker D2 PHASER diffractometer (United States) in the Bragg—Brentano geometry under Cu$K\alpha$ radiation ($\lambda = 1.5406$ Å): the range 2θ from 5° to 90°, step of 0.02°, and an exposure time at each point of 0.1 s. The resulting peaks were approximated with a Lorentzian function using the Jana2006 program [27] to determine their exact position.

The materials were characterized using an FEI Tecnai G2 F20 microscope (United States) equipped with an EDAX energy dispersive attachment (Apollo XLT model) and a Fischione Instruments Model 3000 detector; high resolution transmission electron microscopy (HRTEM) at an accelerating voltage of 80—200 kV and scanning electron microscopy (SEM)

were also used. The particle size distribution was found using the ImageJ program [28]. The statistics was collected for 500 particles.

X-ray absorption near edge structure (XANES) spectra at the K edge of palladium were measured for Pd/CeO_2 at the Structural Materials Science station of the Kurchatov synchrotron radiation source (Moscow, Russia) [29]. A storage ring with an electron-beam energy of 2.5 GeV and a current of 80−100 mA was used as the radiation source. The measurements were carried out in air and without activation in hydrogen. For this purpose, 40 mg of the catalyst powder was placed into a cuvette (the thickness is 3 mm) with kapton windows transparent in the X-ray range. Palladium foil was used as the reference sample and for calibration. The spectra were recorded in the fluorescence mode on a Si(111) monochromator and a solid-state detector, and the palladium foil was measured in the transmission mode. The resulting experimental spectra were processed with the Athena program (Demeter software package) [30].

IR spectra were acquired on a Bruker Vertex 70 spectrometer (United States) equipped with a highly sensitive mercury-telluride detector cooled with liquid nitrogen. A Praying Mantis low-temperature reaction chamber (Harrick Scientific Products Inc., United States) installed in the spectrometer was used for diffuse reflectance Fourier transform infrared spectroscopy measurements. All spectra were recorded with a resolution of 1 cm^{-1} during 64 scans and converted to absorption spectra with the Kubelka−Munk function.

An external gas system equipped with mass flow controllers (EL-FLOW, Bronkhorst High-Tech B.V., Netherlands) was used to control the gas flows (Ar, H_2, and CO passed through a cell and mixed). The experimental equipment made it possible to control the temperature of the sample and gas flow, and it contained a vacuum pump, which made it possible to achieve a pressure inside the volume of the reaction chamber (with the powder sample inside) up to 5×10^{-3} mbar. The experimental procedure involved two stages: activation of the sample and the subsequent low-temperature adsorption/desorption of CO. At the first stage, the samples were heated upon evacuation to 200°C to remove water and other guest molecules, then a flow of hydrogen (5 mL/min) mixed with argon (45 mL/min) was passed through the sample for 30 min to remove oxygen and possible chlorine residues in the case of palladium-containing samples. Finally, the samples were gradually cooled to −140°C with liquid nitrogen as a refrigerant during continuous evacuation for 3 h. Then the sample was purged with a flow of CO (5 mL/min) for 10 min at this temperature. After this procedure, the samples were evacuated, gradually decreasing the CO pressure inside the reaction chamber and, accordingly, the CO coating on the test material. The IR spectra were measured during the overall desorption process. The last spectrum

measured immediately before CO adsorption at low temperature was recorded as the background, which was subtracted from subsequent spectra to avoid any background features not due to the CO adsorption process. The reaction conditions were provided for 2 h for the Pd/CeO_2 sample to obtain data on its stability after functioning under reaction conditions. The sample activated was placed into the reaction chamber at 50°C (the temperature above the maximum observed conversion), whereas a mixture of 16.9% O_2, 62.4% Ar, and 20.7% CO was passed through it at a flow rate of 50 mL/min. Then activation was performed again with the subsequent adsorption of CO.

The catalytic activity was tested in a flow microreactor (a glass tube with an inner diameter of 0.8 mm), into which a mixture of air and CO (16.9% O_2 + 62.4% N_2 + 20.7% CO) was supplied at a pressure of 1 atm. and a flow rate of 20 ml/min. The volumetric flow rate is 120 000 h^{-1}. The O_2/CO molar ratio was 0.82. Catalyst loading was 10 mg. The reactor was heated with an electric furnace, and the temperature was selected and controlled with a Termodat-17 thermostat and a thermocouple placed on the outer wall of the microreactor. The catalyst was activated through heating in a flow of the above mixture up to 300°C (30 min) and cooled to room temperature, stopping the supply of the gases. Then the catalyst was heated at a rate of 10 deg/min, and gaseous products were analyzed at certain temperatures. The measurement was repeated three times to analyze the stability of the Pd/CeO_2 sample and once for all others.

The composition of the initial gas and the gas mixture at the output from the trap were analyzed on a Granat 3700 chromatograph (St. Petersburg, Russia) on two columns filled with NaX molecular sieves ($X = O_2$, N_2, and CO) and HayeSep−Q (air + CO and CO_2). The gas sample was in two circuits of a certain volume, and it was supplied with six-way valves for analysis in real time. A thermal conductivity detector was used at a column temperature of 60°C. Helium was used as the carrier gas.

RESULTS AND DISCUSSION

Elemental Composition

X-ray fluorescence analysis confirmed that there is palladium and/or gold in the samples synthesized. Table 2 shows the concentrations measured. Figures 1 and 2 show the images and distributions of Pd and Au noble metals on the surface of cerium dioxide obtained with TEM and X-ray energy dispersive spectral analysis for monometallic and bimetallic samples, respectively. Palladium is uniformly distributed over the substrate in the case of a Pd/CeO_2 sample (Fig. 1b), and there are no large agglomerates. The particle size distribution is much broader in the Au/CeO_2 sample, and larger gold nanoparticles were found (Fig. 1d). Palla-

Table 2. X-ray fluorescence analysis data

Sample	Theoretical concentration, wt %		Experimental concentration, wt %	
	Pd	Au	Pd	Au
Pd/CeO_2	4	–	2.8	–
Au/CeO_2	–	4	–	4.4
$PdAu/CeO_2$	2	2	1.7	3.1

dium was uniformly distributed in the case of the $PdAu/CeO_2$ bimetallic sample (Fig. 2b), as in the Pd/CeO_2 sample, but gold agglomerates were found (Fig. 2c), albeit smaller than in the Au/CeO_2 sample.

Structure and Size of Particles

Intense peaks in all X-ray powder diffraction patterns confirmed that there is a CeO_2 crystalline substrate (Fig. 3). All diffraction peaks of the CeO_2 substrate material can be assigned to a face-centered cubic lattice of fluorite ($Fm\overline{3}m$ space group, JCPDS No. 34-0394), and the average particle size of 10.8 ± 2.3 nm was assessed from diffraction peaks through the

Debye−Scherrer equation. Neither X-ray powder diffraction patterns nor the initial HRTEM images, however, allowed the identification of palladium nanoparticles both in the case of Pd/CeO_2 monometallic and $PdAu/CeO_2$ bimetallic samples. No Pd or PdO phases were observed on the diffraction patterns of Pd/CeO_2 even after rather long recording of the signal (more than 3 h in a 2θ narrow region from 35° to 45° near the expected position of the most intense Pd 111 reflection). At the same time, larger gold particles on cerium dioxide were clearly visible both in the case of Au/CeO_2 and $PdAu/CeO_2$, which is in agreement with SEM data. This is probably due to the small particle size of palladium, which led to the significant broadening of diffraction peaks characteristic of
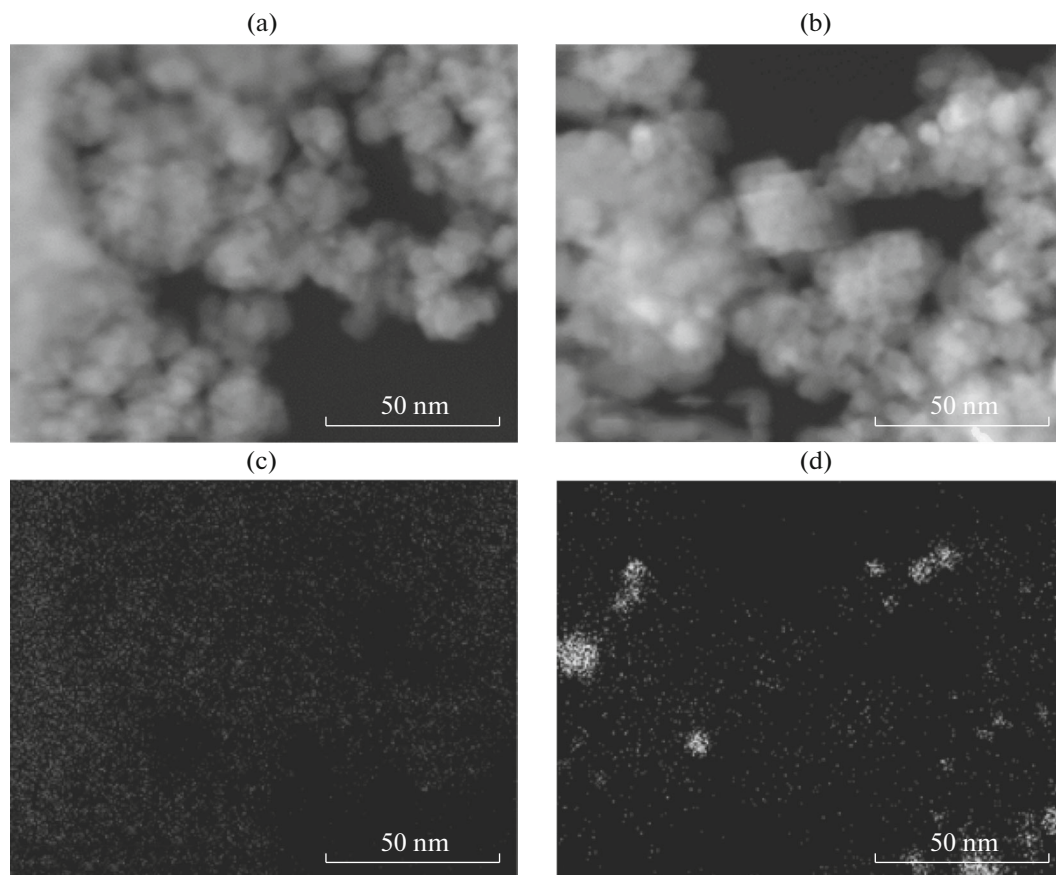

(a)　　　　　　　　　　　　(b)

50 nm　　　　　　　　　　50 nm

(c)　　　　　　　　　　　　(d)

50 nm　　　　　　　　　　50 nm

Fig. 1. TEM images of: (a) Pd/CeO2 and (b) Au/CeO_2; the corresponding distributions of: (c) palladium and (d) gold.
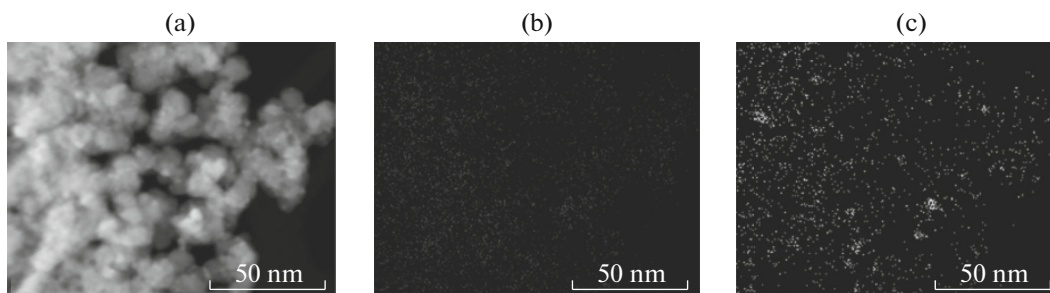
Fig. 2. (a) TEM image of PdAu/CeO$_2$ and the distribution of: (b) palladium and (c) gold.
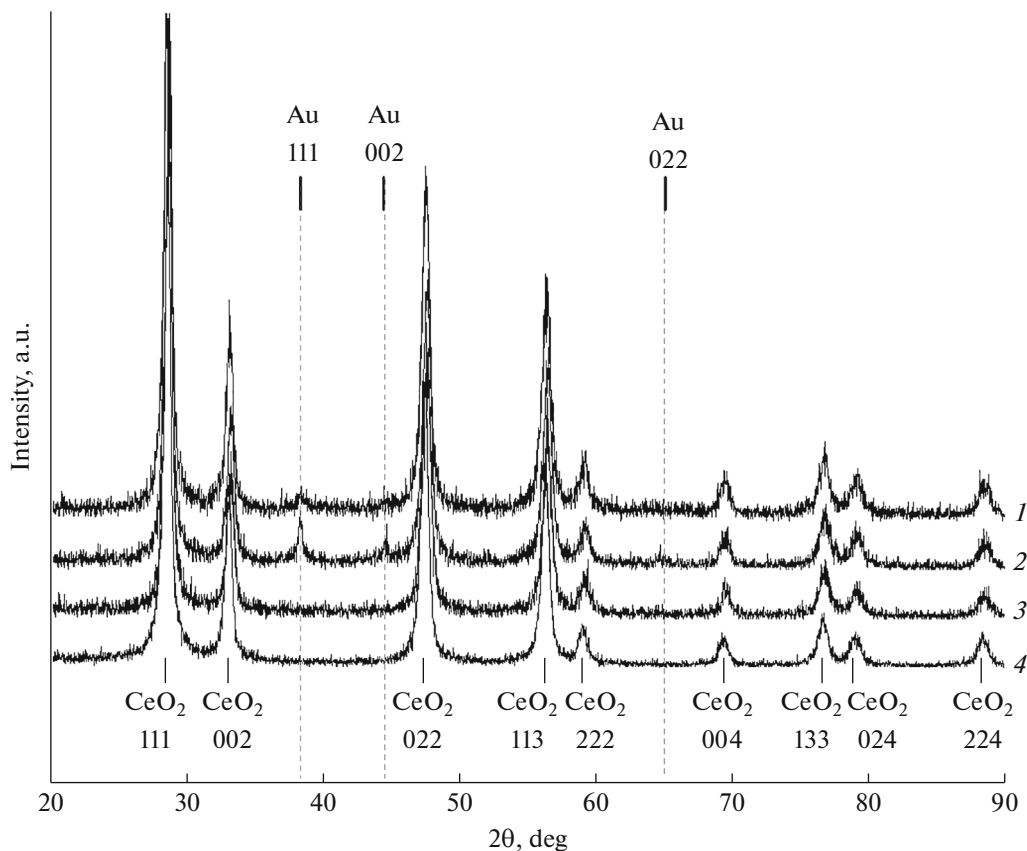

Fig. 3. X-ray powder diffraction patterns of the samples: (*1*) PdAu/CeO$_2$, (*2*) Au/CeO$_2$, (*3*) Pd/CeO$_2$, and (*4*) CeO$_2$ substrate material.

nanoparticles smaller than 4–5 nm [31, 32], or a high dispersion of palladium [33].

Figures 4a–4c show the HRTEM images. They made it possible to describe the nanocrystalline structure of CeO$_2$; however, it was not possible to distinguish palladium nanoparticles from the substrate material in the case of Pd/CeO$_2$ and PdAu/CeO$_2$ because of low Z contrast (Z(Pd) = 46 and Z(Ce) = 58) [34]. All images, with which the reflections and the phases were subsequently identified, were Fourier transformed with ImageJ software [28] to obtain data on phase composition of the samples studied.

Figs. 4d–4f show the initial and transformed images with the most distinct reflections, through which circles with radii corresponding to the interplanar distances were drawn, for all the samples studied. In the case of the Pd/CeO$_2$ sample (Fig. 4d), Fourier transformation made it possible to detect weak reflections due to diffraction at the (111) Pd, d = 0.22(9) nm (JCPDS No. 46–1043), (110) PdO, d = 0.21(1) nm, and (121) PdO planes, d = 0.13(1) nm (JCPDS No. 41–1107). All other brighter spots were assigned to the CeO$_2$ substrate material (JCPDS No. 34-0394). A reflection (besides the strong signal of the substrate
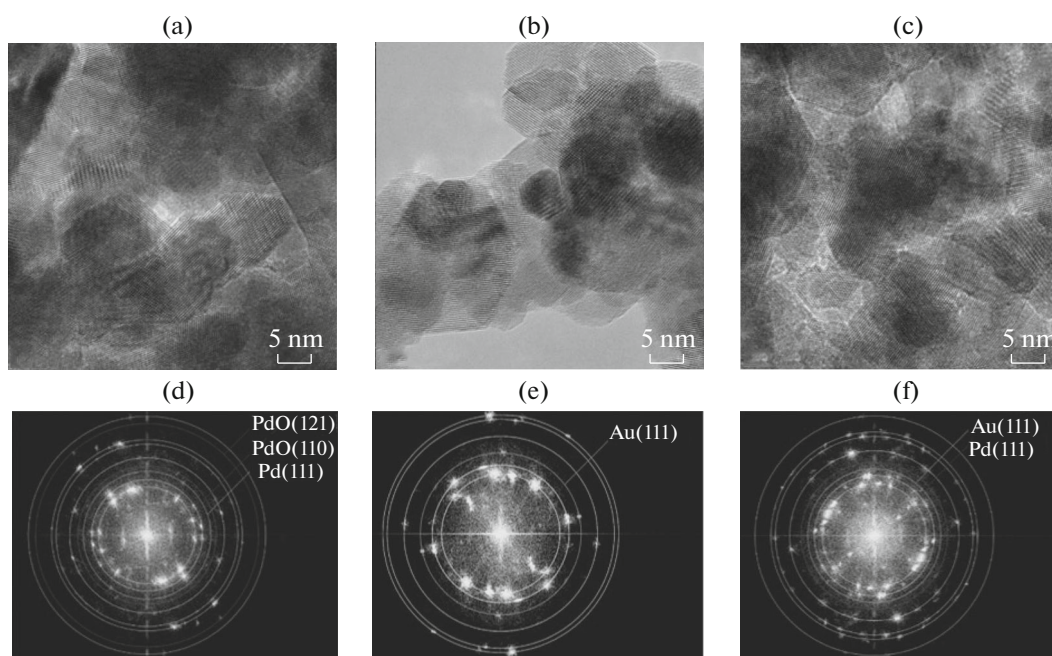
Fig. 4. Initial HRTEM images of: (a) Pd/CeO_2, (b) Au/CeO_2, and (c) $PdAu/CeO_2$ samples and (d–f) their Fourier transformations. The circles were drawn through diffraction reflections due to the Pd, PdO, and Au phases (no CeO_2 phase was designated).

material) assigned to diffraction at the (111) Au planes, $d = 0.23(0)$ nm (JCPDS No. 04-0784), was similarly detected for the Au/CeO_2 sample (Fig. 4e). The signal of the gold and palladium nanoparticles in the diffraction pattern of the $PdAu/CeO_2$ bimetallic sample (Fig. 4f) had a low intensity compared to that of cerium dioxide, which is due to lower loading of each metal separately (Table 2); nevertheless, weak reflections of 111 Pd, $d = 0.21(9)$ nm, and Au, $d = 0.24(1)$ nm, were detected.

Figure 5a shows the XANES spectra measured for a Pd/CeO_2 sample. Palladium foil was used as a bulk reference sample. They underwent Fourier transformation $k^2\chi(k)$ (Fig. 5b). The intense peak at 1.5 Å (without a phase correction) corresponds to Pd–O bonds. The fact that there are Pd–O bonds is in agreement with the HRTEM data, when weak and distinguishable diffraction spots of the PdO phase were observed. Two maxima at 2.5 and 3.0 Å correspond to Pd–Pd bonds, which were both in the unoxidized core of catalyst nanoparticles and on the oxidized surface. There was a significant decrease in the amplitude of the Pd–Pd peak in the Fourier-transformed spectrum of Pd/CeO_2 compared to that of the metal foil, which is probably due to the lower coordination number in the second coordination sphere. Another effect is due to a shift of the Pd–Pd maxima in Pd/CeO_2 towards shorter bond lengths. Both observations indicate that the nanoparticles in the test sample have a small size. Indeed, theoretical simulation [35] implies that the Pd–Pd distances decrease together with the nanoparticle size due to surface relaxation, whereas the coordi-

nation numbers decrease due to the larger surface contribution of the Pd–Pd bonds unsaturated.

Description of Active Centers

Diffuse reflectance Fourier transform infrared spectroscopy combined with the adsorption of CO sample molecules allowed us to obtain information on available active sites and nanoparticle sizes in the $PdAu/CeO_2$ and Pd/CeO_2 samples. Similar measurements were performed for the Au/CeO_2 sample and CeO_2 substrate material to compare and to exclude the possible influence of CO adsorption on the substrate material. CO adsorption on all samples was performed at −140°C after their reduction in the H_2/Ar flow to avoid the formation of surface carbonates, which lead to some electronic effects upon adsorption at cations [36]. An area of 2250–1800 cm^{-1} assigned to vibrational frequencies of linear (L) and bridge (B) carbonyl groups (~2150–2000 and 2000–1800 cm^{-1}, respectively) for palladium, CO molecules adsorbed at the centers of cerium (~2200–2100 cm^{-1}), and gold (~2150–2050 cm^{-1}) were used for analysis in this work. All samples were treated in a reduction hydrogen atmosphere for 30 min at 200°C before adsorption. Three peaks were observed in the carbonyl region (Fig. 6a) with maxima at 2172, 2159, and 2104 cm^{-1} (with the highest CO coverage) in the case of CeO_2 reduced. All these peaks were shifted to the high-frequency region upon a decrease in the CO pressure due to a decrease in the lateral interaction between CO
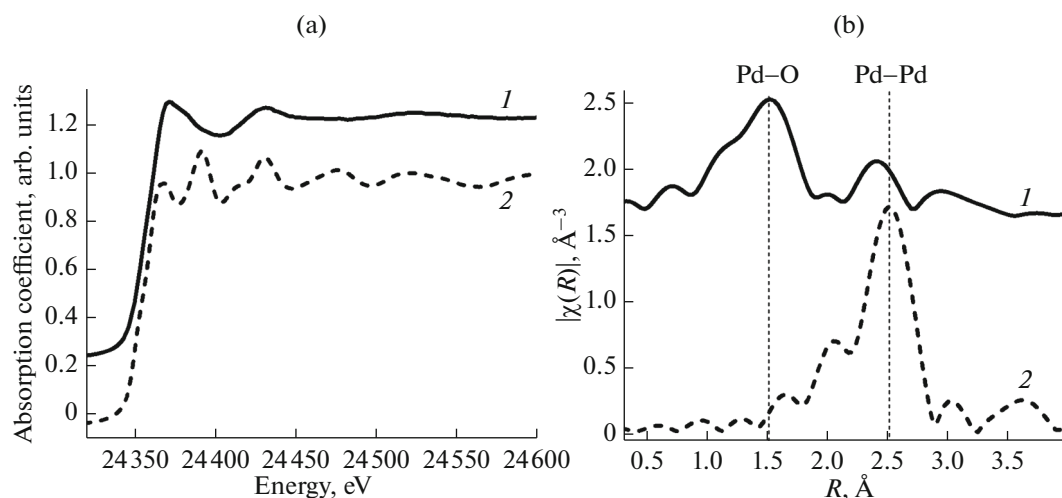
Fig. 5. (a) XANES spectra near the K edge of Pd and (b) their Fourier transformation $k^2\chi(k)$: (*1*) Pd/CeO$_2$ and (*2*) palladium foil. The vertical dashed lines designate the contributions of Pd–O and Pd–Pd coordination shells.

molecules, and they completely disappeared after a pressure of 5×10^{-3} mbar at $-140°$C.

The peak at 2172 cm^{-1} was assigned to CO adsorption at Ce^{4+} centers with coordination unsaturation, which is in good agreement with the literature data for reduced cerium oxide: 2169 [37], 2170 [38], and 2165 cm^{-1} [39]. The peak at 2159 cm^{-1} may be assigned to adsorption at Ce^{4+} with other coordination unsaturation (Ce^{4+} cus), which was observed earlier in the case of unreduced cerium dioxide at 2150 [39], 2156 [40], and 2151 cm^{-1} [36]. Absorption at a similar wavelength during the adsorption of CO on Ce^{3+}, however, was also observed for cerium oxide reduced in hydrogen at 2161 [38], 2162 [41], and 2156 cm^{-1} [42]. The last peak located at 2104 cm^{-1} behaved differently with a decrease in CO coverage during evacuation. It shifted to the low-frequency region in contrast to other peaks, and its value was significantly higher. No such peak is usually mentioned in publications, and its assignment is beyond the scope of this work. Considering that it completely disappeared during desorption at a low temperature, its possible contribution to the absorption spectra after a decrease in CO coating during evacuation of the sample was excluded.

Intense peaks that appeared due to CO adsorption on the substrate material were also observed within 2170–2150 cm^{-1} (at high CO coatings) in the case of the remaining three samples (PdAu/CeO$_2$, Pd/CeO$_2$, and Au/CeO$_2$) (Fig. 6). These peaks completely disappeared after evacuation at $-140°$C. There were two distinct peaks due to CO adsorption at gold nanoparticles in the case of Au/CeO$_2$ (Fig. 6b), besides those due to adsorption at the substrate material. They significantly shifted to the high-frequency region upon evacuation of the sample, up to 2114 and 2129 cm^{-1},

respectively, with minimal CO coverage. The peak at a lower frequency was due to adsorption at centers of metallic gold (Au^0), whereas the high-frequency peak is probably due to adsorption at small gold nanoclusters with a positive charge (Au$^{\delta+}$) [43, 44].

The adsorption of CO on Pd/CeO$_2$ palladium nanoparticles was more complex within 2150–1800 cm^{-1} (Fig. 6c). Two groups of bands were assigned to CO molecules linearly bound to palladium centers designated as L, or linear carbonyls, and to non-linear (bridge) carbonyls designated as B. The first group involved an intense peak with a maximum at about 2108 cm^{-1} having a redshift of up to 2096 cm^{-1} under vacuum, which also had a shoulder in the low-frequency region. The deconvolution results showed that this shoulder is due to a low-frequency peak at 2056 cm^{-1}. The high-frequency peak may be assigned to the linear adsorption of CO on highly dispersed, but not crystalline, palladium particles [45, 46]. The intensity of the low-frequency peak decreased much more slowly than the high-frequency component, which allowed assignment of the peak at 2056 cm^{-1} to the linear adsorption of CO at palladium atoms with a low coordination number, also known as defects (angles, steps, and edges) of Pd (111) crystalline particles. Such behavior during evacuation is in good agreement with the fact that CO is more strongly bound to palladium defects [47]. The adsorption of CO at Pd^{2+} and Pd$^+$ ionic regions could promote absorption at 2170 and 2120 cm^{-1}, respectively [48, 49], but these peaks were not observed during the experiment. When coverage decreased, however, there was a low-intensity peak at 2140 cm^{-1}, which was hidden by a large peak at a frequency of 2108 cm^{-1}. We can assume that this peak is due to single palladium atoms coordinated by oxygen atoms, and simulation results obtained within density

functional theory for the PdO_2/CeO_2 (111) models confirmed this assumption [50], which led to a frequency of 2137 cm^{-1}. The other possible configurations of oxygen-coordinated single atoms on the faces of cerium dioxide, such as PdO/CeO_2 (111) or Pd/CeO_2 (111), should have been located at 2098 and 2047 cm^{-1} according to the results [50], but they overlapped with other peaks in this case.

There were also two main broad absorption peaks: one located at 1960 cm^{-1}, and the second was much wider and was from 1950 to 1850 cm^{-1}. They can be assigned to CO molecules that form bridge carbonyls with two or three palladium atoms, respectively. The intensities of these peaks increased upon evacuation and at a temperature of $-140°C$ (which is more noticeable for the peak assigned to bridge carbonyls bound to two metal atoms) due to the transition of CO molecules from the energetically less favorable positions of linear carbonyls to a bridge coordination [23].

The $PdAu/CeO_2$ bimetallic sample behaved almost identically to that of Pd/CeO_2 during desorption, but the rate with which the intensity decreased was much higher (Fig. 6d). No individual absorption bands corresponding to CO adsorption at gold centers were found, which is due to the lower height of this peak hidden by the more intense and overlapping absorption bands of palladium in the region of linear carbonyls (L). Another explanation is the larger size of gold nanoparticles in a bimetallic sample compared to highly dispersed palladium particles and, as a result, a smaller surface area available for the adsorption of CO sample molecules, which is consistent with the TEM results, where large agglomerates were observed for gold particles.

The particle sizes of Pd/CeO_2 were assessed via deconvolution of the peaks (Fig. 6c) in accordance with the procedure described in [51]. For this purpose, the ratio of the total area under the peaks of CO adsorbed at the bridge sites of palladium (B) and linearly adsorbed CO molecules on palladium (L) was calculated for different CO pressures (CO pressure varied from 7.5 to 5×10^{-3} mbar) at a temperature of $-140°C$. The spectra obtained indicate that this coefficient increases with a decrease in CO coverage, and this fact is in good agreement with published data [23]. The amount of molecules adsorbed at the bridge sites was proportional to the surface area, which corresponds to higher B/L ratios for larger nanoparticles. The particle size, therefore, may be assessed and compared for various structures. The B/L ratio for palladium nanoparticles deposited on TiO_2 corresponds to a size of less than 1.5–2 nm; this indicates a high dispersion of palladium nanoparticles in the test sample [52].

The size was similarly assessed for a $PdAu/CeO_2$ bimetallic sample. Deconvolution of the spectrum (Fig. 6d) at a pressure of $P_{CO} = 5 \times 10^{-3}$ mbar (after 10 min of evacuation) showed that the ratio of the
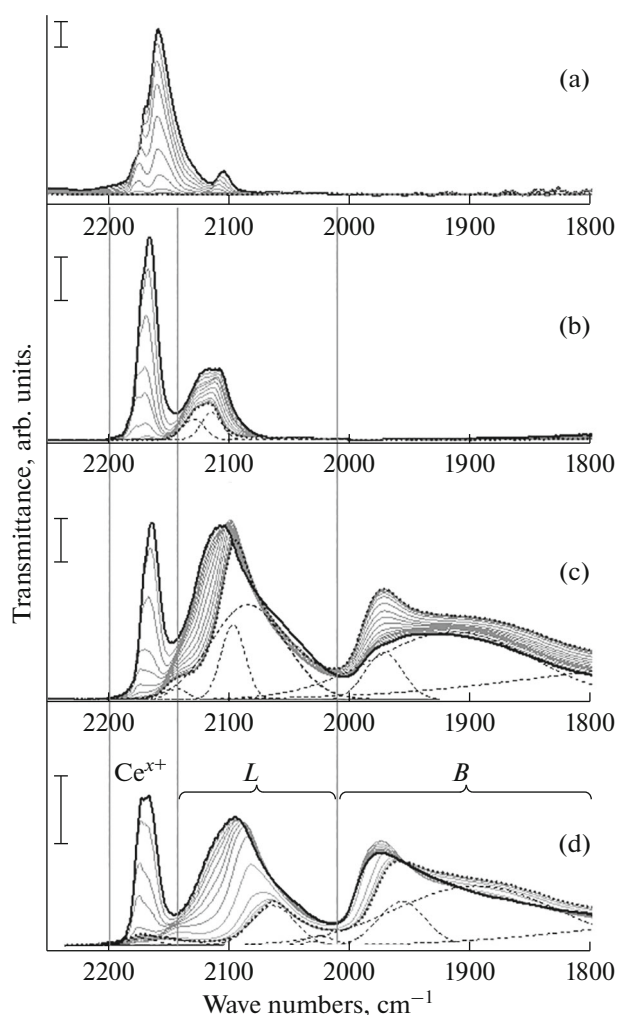

Fig. 6. IR spectra measured during the desorption of CO at $-140°C$ reduced previously at 200°C in 5% H_2/Ar mixture: (a) CeO_2, (b) Au/CeO_2, (c) Pd/CeO_2, and (d) $PdAu/CeO_2$. The spectrum measured with the largest CO coverage ($P_{CO} = 4-8$ mbar) is highlighted with a solid black bold line; a series of spectra obtained via a decrease in CO coverage is shown in gray; the spectrum after continuous evacuation for 10 min ($P_{CO} = 5 \times 10^{-3}$ mbar) is designated with a dotted line. The dashed line designates the approximation results of spectra using the Gaussian function.

areas under the B/L peaks was 6.52, which is much higher than that obtained in a similar way and under completely identical conditions for Pd/CeO_2 (1.42). In addition, if we compare the size of palladium nanoparticles exclusively, it is also necessary to subtract the contribution of CO adsorption at gold centers to the total area under the peaks of linear carbonyls (L) for a more accurate assessment. Taking this contribution into account, however, will only lead to a decrease in the area under the absorption peaks of linear carbonyls at palladium centers, so that B/L will only increase. This leads to the conclusion that the size of the palladium nanoparticles in this sample is larger
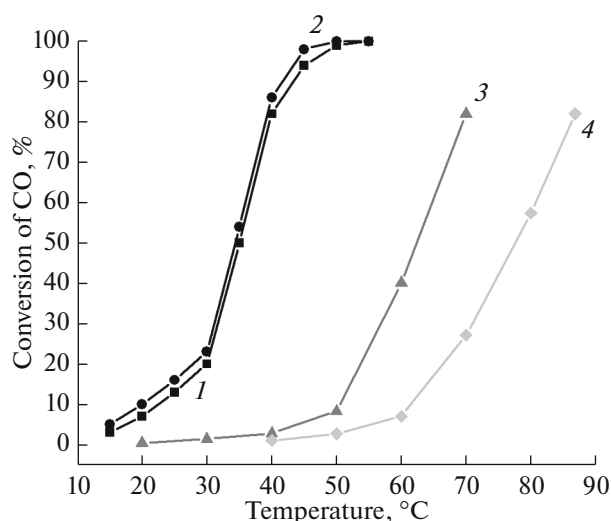
Fig. 7. Relationship between CO conversion and temperature, at which the oxidation reaction proceeds in a mixture of 16.9% O_2, 62.4% N_2, and 20.7% CO at a flow rate of 120 000 h^{-1}: (*1*) the first and (*2*) third cycles for the Pd/CeO$_2$ sample, (*3*) one cycle for the Au/CeO$_2$ sample, and (*4*) one cycle for the PdAu/CeO$_2$ sample. The molar ratio of gases in the mixture O_2/CO is 0.82.

than that for the Pd/CeO$_2$ one and is within 3–4 nm or even higher [52]. After catalytic tests of the Pd/CeO$_2$ sample, the ratio of the areas under the peaks of nonlinear and linear carbonyls remained unchanged with an accuracy of 2.8% (the spectra are not shown, because they are completely similar to the initial spectrum). There were slight changes in the relative intensities for nonlinear carbonyls at diatomic and triatomic palladium centers. The latter indicates reorganization of the surface of the nanoparticles, whereas the average size found from the *B/L* ratio remained almost unchanged.

Catalytic Activity

The Pd/CeO$_2$ sample possessed a high catalytic activity: there was a 10% conversion already at room temperature and it increased up to 100% at ~50°C (Fig. 7). For comparison, the Au/CeO$_2$ sample achieved 82% conversion only at 70°C. The activity of the bimetallic sample was lower, and comparable conversion values were achieved at an even higher temperature. Such a high catalytic activity of the materials is probably due to the strong interaction of palladium or gold with the CeO$_2$ surface and the large oxygen storage capacity to form a Ce^{4+}/Ce^{3+} redox pair, which allows CeO$_2$ to efficiently release catalytically active oxygen atoms [21, 53]. It is known that gold and palladium nanoparticles with their identical size and concentration should exhibit close catalytic activity [2]. The differences in the activity of the materials synthesized are due to a boundary effect of the nanoparticle

perimeter [54, 55]. The size of palladium clusters on average is less than 2 nm, whereas gold nanoparticles are much larger. Smaller palladium clusters maximize the contact area between the metal particles and the transition-metal-oxide substrate to minimize the area of "free" palladium nanoparticles. A decrease in the size of palladium nanoparticles also leads to an increase in the amount of active sites on their surface. As a result, the Pd/CeO$_2$ sample possesses a higher catalytic activity compared to those of Au/CeO$_2$ and PdAu/CeO$_2$.

The published data showed that some previous similar systems have significantly less catalytic activity. Indeed, carbon monoxide was completely oxidized with palladium nanoparticles on various substrates only at temperatures from 110 to 250°C [2, 3, 7]. Gold nanoparticles possess a similar catalytic activity, but slightly less than that of a palladium catalyst [3]. Similar CO conversion values are characteristic for the temperature range of 150–250°C. The conversion of CO on a bimetallic (PdAu) catalyst was also reported [56]. The temperature of a complete conversion of the nanoparticles on the surface of SiO$_2$ was 140°C, whereas it was 60°C on the surface of TiO$_2$. Such a significant difference is due to the fact that the SiO$_2$ substrate cannot act as an active oxygen donor because of the high degree of inertness of silicon oxide(IV) to reduction processes. Activation proceeds exclusively on the surface of metal nanoparticles. This leads to competition in parallel processes of the activation of CO and O$_2$, which decreases the catalytic activity. The TiO$_2$ substrate is capable of supplying activated oxygen due to the ease of redox processes Ti^{4+}/Ti^{3+} and the formation of a TiO$_{2-x}$ non-stoichiometric oxide. The low catalytic activity of the bimetallic sample studied in this work is probably due to the larger sizes of the nanoparticles.

Materials with low-temperature catalytic activity are also discussed; for example, the data mentioned in [5, 6, 8] are similar to those obtained in this work for the Pd/CeO$_2$ sample. Such a difference in temperatures of complete conversion is probably due to the arrangement of metal nanoparticles on different CeO$_2$ surfaces: (100) or (111). The authors showed that transformation at low temperatures requires that metal nanoparticles should be on the (111) substrate surface, whereas the transformation on the (100) surface proceeds at higher temperatures [7]. They also found that palladium on the (111) surface of cerium dioxide possesses higher activity due to the Langmuir–Hinshelwood bimolecular mechanism. Microkinetic simulations of the catalytic CO oxidation cycles within density functional theory and the calculated reaction rates show that CO oxidation for the (100) CeO$_2$ surface proceeds in accordance with the Mars–Van Krevelen mechanism. This effect is probably due to the lower Ce–O bond energy compared to that of the (111) sur-

face. Generally, the catalytic mechanism of CO oxidation on Pd/CeO_2 (100) implies a higher free energy barrier than that on Pd/CeO_2 (111) according to the experimental difference in activity. As a result, the high catalytic activity of the materials discussed in this work is due to a large amount of metal nanoparticles located on the (111) CeO_2 surface and indirectly indicates the Langmuir–Hinshelwood catalytic mechanism.

CONCLUSIONS

Palladium and gold monometallic nanoparticles together with a palladium-gold bimetallic system on a modified cerium-dioxide substrate were synthesized in this work. The Pd/CeO_2 sample possessed the highest catalytic activity in the CO oxidation reaction and the thermal stability during cyclic tests: complete conversion was already achieved at 50°C. The catalytic activity of the Au/CeO_2 and $PdAu/CeO_2$ samples was lower; no synergistic effect was observed in the case of a bimetallic sample.

IR Fourier spectroscopy together with CO reference molecules was used to describe the samples because of low Z contrast and the small size of noble-metal nanoparticles. The vibrational frequencies characteristic of nonlinear carbonyls formed during CO adsorption on two and three palladium atoms showed that there are ultrafine nanoparticles, but not single palladium atoms on the surface of Pd/CeO_2 and $PdAu/CeO_2$ samples. The ratio of the areas under the peaks corresponding to nonlinear and linear carbonyls made it possible to assess the average size of palladium nanoparticles, which was less than 1.5–2 nm in the case of monometallic and more than 3–4 nm for the bimetallic sample. This was in agreement with the TEM and XANES data and the results of catalytic tests. The possible dominance of the surface faces of CeO_2 (111) can also explain the high catalytic activity.

FUNDING

REFERENCES

1. Z. Tang, J. Edwards, J. Bartley, et al., J. Catal. **249** (2), 208 (2007).
https://doi.org/10.1016/j.jcat.2007.04.016

2. Y. Yang, K. M. Saoud, V. Abdelsayed, et al., Catal. Commun. **7** (5), 281 (2006).
https://doi.org/10.1016/j.catcom.2005.11.014

3. G. Glaspell, L. Fuoco, and M. S. El-Shall, J. Phys. Chem. B **109,** 17350 (2005).
https://doi.org/10.1021/jp0526849

4. J. Zou, Z. Si, Y. Cao, et al., J. Phys. Chem. C **120** (51), 29116 (2016).
https://doi.org/10.1021/acs.jpcc.6b08630

5. H. Jeong, J. Bae, J. W. Han, et al., ACS Catal. **7** (10), 7097 (2017).
https://doi.org/10.1021/acscatal.7b01810

6. E. M. Slavinskaya, R. V. Gulyaev, A. V. Zadesenets, et al., Appl. Catal., B **166−167,** 91 (2015).
https://doi.org/10.1016/j.apcatb.2014.11.015

7. G. Spezzati, A. D. Benavidez, A. T. DeLaRiva et al., Appl. Catal., B **243,** 36 (2019).
https://doi.org/10.1016/j.apcatb.2018.10.015

8. H. Zhu, Z. Qin, W. Shan, et al., J. Catal. **233,** 41 (2005).
https://doi.org/10.1016/j.jcat.2005.04.033

9. K. J. Kinoshita, J. Electrochem. Soc. **137** (3), 845 (1990).
https://doi.org/10.1149/1.2086566

10. S. Rojluechai, S. Chavadej, J. W. Schwank, et al., Catal. Commun. **8** (1), 57 (2007).
https://doi.org/10.1016/j.catcom.2006.05.029

11. M. L. Buil, M. A. Esteruelas, S. Niembro, et al., Organometallics **29** (19), 4375 (2010).
https://doi.org/10.1021/om1003072

12. J. Shim, D. -Y. Yoo, and J. -S. Lee, Electrochim. Acta **45** (12), 1943 (2000).
https://doi.org/10.1016/S0013-4686(99)00414-4

13. L. Nie, D. Mei, H. Xiong, et al., Science **358** (6369), 1419 (2017).
https://doi.org/10.1126/science.aao2109

14. M. Guo, C. Li, and Q. Yang, Catal. Sci. Technol **7** (11), 2221 (2017).
https://doi.org/10.1039/C7CY00394C

15. Z. Li, J. Liu, C. Xia, et al., ACS Catal. **3** (11), 2440 (2013).
https://doi.org/10.1021/cs400506q

16. A. Wong, Q. Liu, S. Griffin, et al., Science **358** (6369), 1427 (2017).
https://doi.org/10.1126/science.aao6538

17. J. Wei, L. Zou, and Y. Li, J. Porous Mater. **26,** 157 (2018).
https://doi.org/10.1007/s10934-018-0632-1

18. S. Chaudhary, P. Sharma, D. Singh, et al., ACS Sustainable Chem. Eng. **5** (8), 6803 (2017).
https://doi.org/10.1021/acssuschemeng.7b01041

19. J. Xu, L. Li, and G. Li, J. Dispersion Sci. Technol. **29** (8), 1072 (2008).
https://doi.org/10.1080/01932690701815879

20. A. B. Jorge, Y. Sakatani, C. Boissière, et al., J. Mater. Chem. **22** (7), 3220 (2012).
https://doi.org/10.1039/c2jm15230d

21. Q. Fu, A. Weber, and M. Flytzani-Stephanopoulos, Catal. Lett. **77** (1), 87 (2001).
https://doi.org/10.1023/A:1012666128812

22. O. V. Safonova, A. A. Guda, C. Paun, et al., J. Phys. Chem. C **118** (4), 1974 (2014).
https://doi.org/10.1021/jp409571b

23. E. Groppo, S. Bertarione, F. Rotunno, et al., J. Phys. Chem. C **111** (19), 7021 (2007).
https://doi.org/10.1021/jp0666434

24. C. Lamberti, A. Zecchina, E. Groppo, et al., Chem. Soc. Rev. **39** (12), 4951 (2010).
https://doi.org/10.1039/C0CS00117A

25. H. L. Abbott, A. Aumer, Y. Lei, et al., J. Phys. Chem. C **114** (40), 17099 (2010).
https://doi.org/10.1021/jp1038333

26. C. Benmouhoub, A. Kadri, N. Benbrahim, et al., Mater. Sci. Forum **609,** 189 (2009) doi 10.4028/www.scientific.net/MSF.609.189

27. V. Petříček, M. Dušek, and L. Palatinus, Z. Kristallogr. **229** (5), 345 (2014).
https://doi.org/10.1515/zkri-2014-1737

28. C. A. Schneider, W. S. Rasband, and K. W. Eliceiri, Nat. Methods **9,** 671 (2012).
https://doi.org/10.1038/nmeth.2089

29. A. A. Chernyshov, A. A. Veligzhanin, and Ya. V. Zubavichus, Nucl. Instrum. Methods Phys. Res. A **603,** 95 (2009).

30. B. Ravel and M. Newville, J. Synchrotron Radiat. **12,** 537 (2005).
https://doi.org/10.1107/S0909049505012719

31. A. Baylet, P. Marécot, D. Duprez, et al., Phys. Chem. Chem. Phys. **13** (10), 4607 (2011).
https://doi.org/10.1039/C0CP01331E

32. W. Zhou and J. Y. Lee, J. Phys. Chem. C **112** (10), 3789 (2008).
https://doi.org/10.1021/jp077068m

33. Y. Xia, J. Ye, D.-G. Cheng, et al., Catal. Sci. Technol. **8** (20), 5137 (2018).
https://doi.org/10.1039/C8CY01590B

34. M. Cargnello, T. Montini, S. Polizzi, et al., Dalton Trans. **39** (8), 2122 (2010).
https://doi.org/10.1039/B916035C

35. W. Qi, B. Huang, and M. Wang, Nanoscale Res. Lett. **4** (3), 269 (2009).
https://doi.org/10.1007/s11671-008-9236-z

36. C. Binet, M. Daturi, and J.-C. Lavalley, Catal. Today **50** (2), 207 (1999).
https://doi.org/10.1016/S0920-5861(98)00504-5

37. M. I. Zaki and H. Knözlngem, Spectrochim. Acta, Part A **43** (12), 1455 (1987).
https://doi.org/10.1016/S0584-8539(87)80030-2

38. A. Badri, C. Binet, and J.-C. Lavalley, J. Chem. Soc., Faraday Trans. **92** (9), 1603 (1996).
https://doi.org/10.1039/FT9969201603

39. F. Bozon-Verduraz and A. Bensalem, J. Chem. Soc., Faraday Trans. **90** (4), 653 (1994).
https://doi.org/10.1039/FT9949000653

40. C. Li, Y. Sakata, T. Arai, et al., J. Chem. Soc., Faraday Trans. **85** (4), 929 (1989).
https://doi.org/10.1039/F19898500929

41. K. Mudiyanselage, H. Y. Kim, S. D. Senanayake, et al., Phys. Chem. Chem. Phys. **15** (38), 15856 (2013).
https://doi.org/10.1039/C3CP52295D

42. S. Chen, T. Cao, Y. Gao, et al., J. Phys. Chem. C **120** (38), 21472 (2016).
https://doi.org/10.1021/acs.jpcc.6b06158

43. M. Manzoli, F. Boccuzzi, A. Chiorino, et al., J. Catal. **245,** 308 (2007).
https://doi.org/10.1016/j.jcat.2006.10.021

44. T. Tabakova, F. Boccuzzi, M. Manzoli, et al., Appl. Catal., A **252,** 385 (2003).
https://doi.org/10.1016/S0926-860X(03)00493-9

45. J. M. Padilla, G. Del Angel, and J. Navarrete, Catal. Today **133-135,** 541 (2008).

46. F. Di Gregorio, L. Bisson, T. Armaroli, et al., Appl. Catal., A **352** (1), 50 (2009).
https://doi.org/10.1016/j.apcata.2008.09.034

47. I. V. Yudanov, R. Sahnoun, K. M. Neyman, et al., J. Phys Chem. B **107** (1), 255 (2003).
https://doi.org/10.1021/jp022052b

48. X. Wang, G. Wu, N. Guan, et al., Appl. Catal., B **115−116,** 7 (2012).
https://doi.org/10.1016/j.apcatb.2011.12.011

49. T. Baidya, P. Bera, B. Mukri, et al. J. Catal. **303,** 117 (2013).
https://doi.org/10.1016/j.jcat.2013.03.020

50. G. Spezzati, Y. Su, J. P. Hofmann, et al., ACS Catal. **7** (10), 6887 (2017).
https://doi.org/10.1021/acscatal.7b02001

51. L. Sheu, Z. Karpinski, and W. M. H. Sachtler, J. Phys. Chem. **93** (12), 4890 (1989).
https://doi.org/10.1021/j100349a042

52. Q. Fan, S. He, L. Hao, et al., Sci. Rep. **7,** 42172 (2017).
https://doi.org/10.1038/srep42172

53. A. Iglesias-Juez, A. B. Hungria, A. Martinez-Arias, et al., Catal. Today **143** (3), 195 (2009).
https://doi.org/10.1016/j.cattod.2008.12.013

54. J. Qi, J. Chen, G. Li, et al., Energy Environ. Sci **5** (10), 8937 (2012).
https://doi.org/10.1039/c2ee22600f

55. M. Cargnello, V. V. Doan-Nguyen, T. R. Gordon, et al., Science **341** (6147), 771 (2013).
https://doi.org/10.1126/science.1240148

56. L. Guczi, A. Beck, A. Horvath, et al., J. Mol. Catalysis. A: Chem. **204−205,** 545 (2003).
https://doi.org/10.1016/S1381-1169(03)00337-6

Translated by A. Tulyabaev